

# Ab Initio Molecular Dynamics Investigation of the Concentration Dependence of Charged Defect Transport in Basic Solutions via Calculation of the Infrared Spectrum<sup>†</sup>

Zhongwei Zhu<sup>‡</sup> and Mark E. Tuckerman<sup>\*,‡,§</sup>

Department of Chemistry, and Courant Institute of Mathematical Sciences, New York University,  
New York, New York 10003

Received: April 2, 2002

The concentration dependence of the anomalous proton transport mechanism in aqueous KOD solution is studied using ab initio molecular dynamics. A high concentration of 13 M is chosen because of the availability of Raman and infrared spectroscopic data at this concentration. Differences in certain features of these spectra have been interpreted in terms of the so-called “proton hole” picture of the proton transport mechanism in basic solutions. The proton hole mechanism asserts that the charged defect transport in basic solutions follows the same mechanism as in acidic solutions (where the charged defect is  $\text{H}_3\text{O}^+$ ) with all of the hydrogen-bond polarities reversed. By computing the infrared spectrum directly from an ab initio molecular dynamics simulation, we are able to validate our ab initio approach against the experimental data. However, the mechanism of charged defect transport that emerges from the simulation is considerably different from the proton hole mechanism and follows that recently reported by Tuckerman, et al. (Tuckerman, M. E.; Marx, D.; Parrinello, M. *Nature* 2002, 417, 925). For comparison, a lower concentration, 1.5 M, is also simulated and the transport mechanism compared to the high concentration case. It is found that the mechanisms are similar; however, the mobility of both  $\text{K}^+$  and  $\text{OD}^-$  is slower at high concentration, a finding that is in keeping with the fact that the molar conductivity of electrolytes decreases with increasing concentration. Other similarities and differences between the two concentrations are highlighted, and a new interpretation of the spectral data is proposed.

## 1. Introduction

Understanding the behavior of charged defects in aqueous environments created by the addition or removal of protons is of fundamental importance the chemistry of acids and bases, in biological processes such as proton transport across lipid membranes,<sup>1–5</sup> and in industrially and technologically important applications such as fuel cell operation.<sup>6,7</sup> It is well known that such charged defects have an unusually high mobility in aqueous solution, a fact that is regarded as one of water’s anomalous properties. The high mobility of both hydronium ( $\text{H}_3\text{O}^+$ ) and hydroxide ( $\text{OH}^-$ ) ion defects presents a considerable challenge, both theoretically and experimentally, in identifying their microscopic transport mechanisms. Extensive investigations,<sup>8–31</sup> have ultimately led to a clear understanding of the transport mechanism of  $\text{H}_3\text{O}^+$  in aqueous acidic solution. The mechanism that has emerged<sup>16–18</sup> is one of a continuous interconversion between two solvation complexes. Specifically, a tricoordinate  $\text{H}_3\text{O}^+(\text{H}_2\text{O})_3$  or  $\text{H}_9\text{O}_4^+$  complex, in which an  $\text{H}_3\text{O}^+$  core donates three hydrogen bonds to neighboring waters, is transformed via proton transfer into a  $[\text{H}_2\text{O}\cdots\text{H}^+\cdots\text{OH}_2]$  or  $\text{H}_5\text{O}_2^+$  complex, in which the excess proton is shared equally between two water molecules. Nuclear quantum effects, which give rise to a significant delocalization of the defect structures, lead to a picture in which the complexes are viewed as highly “fluxional” defects in the hydrogen bond network.<sup>25</sup> The transport mechanism, known as the “structural diffusion” or “Grotthuss” mechanism,<sup>32</sup> is driven by a hydrogen-bond breaking event in

the second solvation shell of  $\text{H}_3\text{O}^+$  that reduce the coordination of a first solvation shell water from four to three.<sup>16–18</sup> When undercoordinated, this water has a solvation structure characteristic of  $\text{H}_3\text{O}^+$  and is, thus, “prepared” to become a properly solvated  $\text{H}_3\text{O}^+$  via proton transfer. This process is illustrated in Figure 1.

In stark contrast to the case of solvated  $\text{H}_3\text{O}^+$ , far less is known about the behavior of  $\text{OH}^-$  in aqueous solution. This is surprising considering that basic solutions are no less important than their acidic counterparts. Indeed, basic solutions and base catalysis play important roles in organic syntheses such as aldol addition and the aqueous Wittig reaction,<sup>33</sup> in biochemical processes such as glycolysis, fermentation, and hydrolysis of  $\text{CO}_2$  by carbonic anhydrase,<sup>34–36</sup> and in industrial processes such as saponification.<sup>33</sup> The reason  $\text{OH}^-$  transport has received less attention is due to a century-old notion<sup>37</sup> that views  $\text{OH}^-$  as a water molecule with a missing proton or “proton hole.” In this picture, which was later exploited by Hückel,<sup>38</sup> it is assumed that the transport mechanism of  $\text{OH}^-$  can be deduced from that of  $\text{H}_3\text{O}^+$  by simply reversing the hydrogen bond polarities. Thus, by analogy with the  $\text{H}_3\text{O}^+$  case, one would expect the  $\text{OH}^-$  transport process to involve a continuous interconversion between a tricoordinate ( $\text{H}_7\text{O}_4^-$ ) complex in which  $\text{OH}^-$  accepts three hydrogen bonds (one for each electron lone pair) and a  $[\text{HO}\cdots\text{H}^+\cdots\text{OH}^-]$  or  $\text{H}_3\text{O}_2^-$  complex in which the proton is shared equally between two  $\text{OH}^-$  moieties. Just as  $\text{H}_5\text{O}_2^+$  is relatively stable in acidic solution, one would expect that  $\text{H}_3\text{O}_2^-$  should also be stable in basic solution.<sup>39</sup> Also, by analogy with the  $\text{H}_3\text{O}^+$  case, one would expect a second solvation shell fluctuation that changes the coordination of a first solvation shell water from four to three would prepare the water to transfer

<sup>†</sup> Part of the special issue “John C. Tully Festschrift.”

<sup>\*</sup> Corresponding author.

<sup>‡</sup> Department of Chemistry.

<sup>§</sup> Courant Institute of Mathematical Sciences.

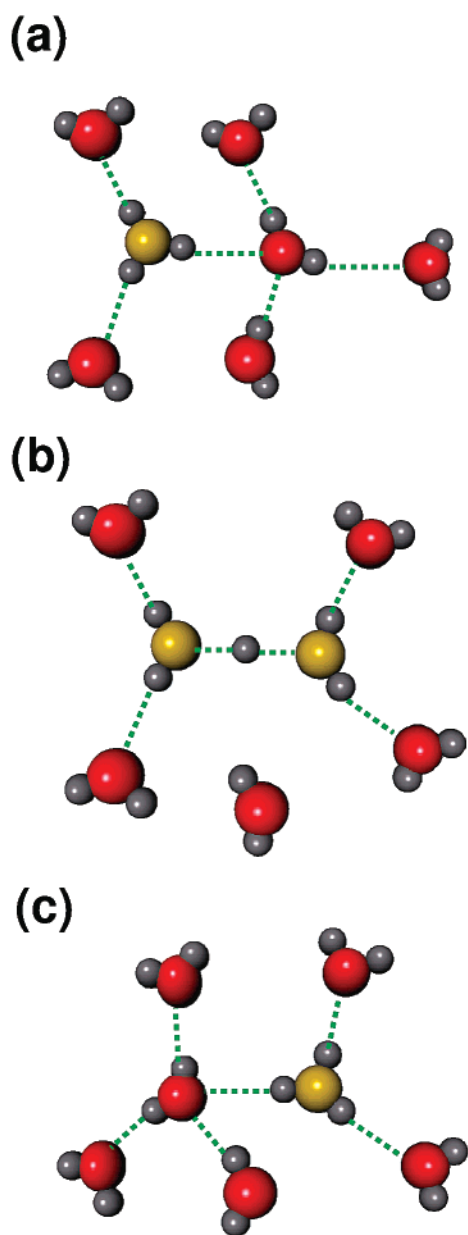


**Figure 1.** Illustration of the structural diffusion mechanism of  $\text{H}_3\text{O}^+$  in water.<sup>16–18</sup> Oxygens are represented as red spheres, hydrogens as gray spheres. The hydronium oxygen is represented as a yellow sphere. Panel (a) shows the hydronium ion in a 3-fold coordination state, and the full 4-fold coordination pattern of one of the first solvation shell waters is shown. In panel (b), a hydrogen bond breaking event between first and second solvation shell members of  $\text{H}_3\text{O}^+$  is followed by a slight shrinking of one of the oxygen–oxygen distances between  $\text{H}_3\text{O}^+$  and the first solvation shell water. The excess proton moves to the center of this hydrogen bond forming an intermediate  $\text{H}_5\text{O}_2^+$  complex. If the proton is fully transferred to the first solvation shell water molecule (panel c), then a properly solvated  $\text{H}_3\text{O}^+$  is formed. The “gate closes” if the original hydronium (now a water molecule) captures a nearby water to complete its solvation shell. Although this process is shown using the water released from the second solvation shell in panel (b), it could be any nearby solvent water.

one of its protons to the  $\text{OH}^-$ , thus transforming it into a properly solvated  $\text{OH}^-$ . Finally, it is assumed that the hydroxide hydrogen does not donate a hydrogen bond to a nearby water (in the same way that the single lone electron pair in  $\text{H}_3\text{O}^+$  does not generally accept a hydrogen bond from a nearby water). Indeed, such a mechanism has recently been proposed.<sup>39</sup> While some experimental data, e.g., measured IR and Raman spectra

of aqueous KOH and NaOD solutions,<sup>40–42</sup> appear to support this mechanism, other experimental data, e.g., gas-phase spectroscopy<sup>43</sup> and estimated coordination numbers,<sup>44</sup> and quantum chemical calculations,<sup>45</sup> all of which indicate a high  $\text{OH}^-$  coordination numbers in solution, appear to be at odds with the proton hole picture, which assumes that the tricoordinate ( $\text{H}_7\text{O}_4^-$ ) and  $\text{H}_3\text{O}_2^-$  complexes are the most stable in solution. The key spectroscopic feature that is thought to support the proton hole mechanism is a sharp peak in the Raman spectrum at  $3600\text{ cm}^{-1}$  for 14 M KOH solution ( $2660\text{ cm}^{-1}$  for 14 M KOD solution), which is highly suppressed in the IR spectrum.<sup>42</sup> It has been suggested that the prominent Raman peak, which is assigned to a free OH stretch in a hydroxide moiety, indicates the presence of a highly symmetric  $\text{H}_3\text{O}_2^-$  complex in which the two OH moieties point in nearly opposite directions.<sup>39,42</sup> Such a structure would ostensibly explain the lack of a signal in the IR spectrum, as the contributions to the change in the dipole moment due to symmetric stretching would tend to cancel out. An important caveat is that the IR and Raman spectra are measured in highly concentrated solutions and, therefore, may not apply to ordinary concentrations where the proton hole transport mechanism is assumed to hold.

Recently, we have introduced an alternative to the proton hole mechanism,<sup>31</sup> deduced directly from extensive ab initio path integral simulations<sup>46,47</sup> of a single  $\text{OH}^-$  in a bath of 32 water molecules. As in our previous ab initio MD simulations with classical nuclei,<sup>16,17</sup> two dominant solvation complexes emerge. Specifically, a complex is found in which the hydroxide oxygen accepts four hydrogen bonds from neighboring waters in a roughly planar arrangement, forming a  $\text{OH}^-(\text{H}_2\text{O})_4$  or  $\text{H}_9\text{O}_5^-$  structure. The second complex is a tricoordinate complex, in which the hydroxide oxygen accepts three hydrogen bonds in a tetrahedral arrangement, forming a  $\text{OH}^-(\text{H}_2\text{O})_3$  or  $\text{H}_7\text{O}_4^-$  structure. In addition, it is found that the hydroxide hydrogen participates in a relatively weak hydrogen bond that plays an important role in the transport mechanism. The average coordination number of  $\text{OH}^-$  is found to be between 4 and 5, which agrees with experimental estimates,<sup>44</sup> gas-phase spectroscopic measurements,<sup>43</sup> and quantum chemical calculations.<sup>45</sup> The transport mechanism is found to involve a transformation from the  $\text{H}_9\text{O}_5^-$  to the  $\text{H}_7\text{O}_4^-$  structure by breaking a first solvation shell hydrogen bond followed by the formation of a hydrogen bond between the  $\text{OH}^-$  hydrogen and a neighboring water. These events leave the  $\text{OH}^-$  with a roughly tetrahedral coordination pattern in which it accepts three hydrogen bonds and donates one, a pattern characteristic of that of a water molecule. In this way it is thus “prepared” to become a properly solvated water via proton transfer through one of its accepting hydrogen bonds. The process is illustrated in Figure 2. This mechanism has also been shown to be consistent with the observed activation enthalpy.<sup>48,49</sup> Indeed, considering this proposed transport mechanism and that of  $\text{H}_3\text{O}^+$  leads to the notion that proton transfer can occur when the proton-receiving species is “pre-solvated” via fluctuations, like the species it will become as a result of proton transfer.<sup>31</sup> This “rule” has also been applied by us, in conjunction with ab initio molecular dynamics simulations, to explain the anomalously high mobility of protons in liquid methanol<sup>50</sup> and to explain the lack of proton transfer in liquid ammonia.<sup>51</sup>

The fact that the mechanism described above differs from the proton hole mechanism and yet is consistent with coordination number,<sup>44</sup> gas-phase data,<sup>43</sup> and quantum chemical calculations<sup>45</sup> naturally raises the question of whether it is also consistent with the spectroscopic data and, if so, whether another

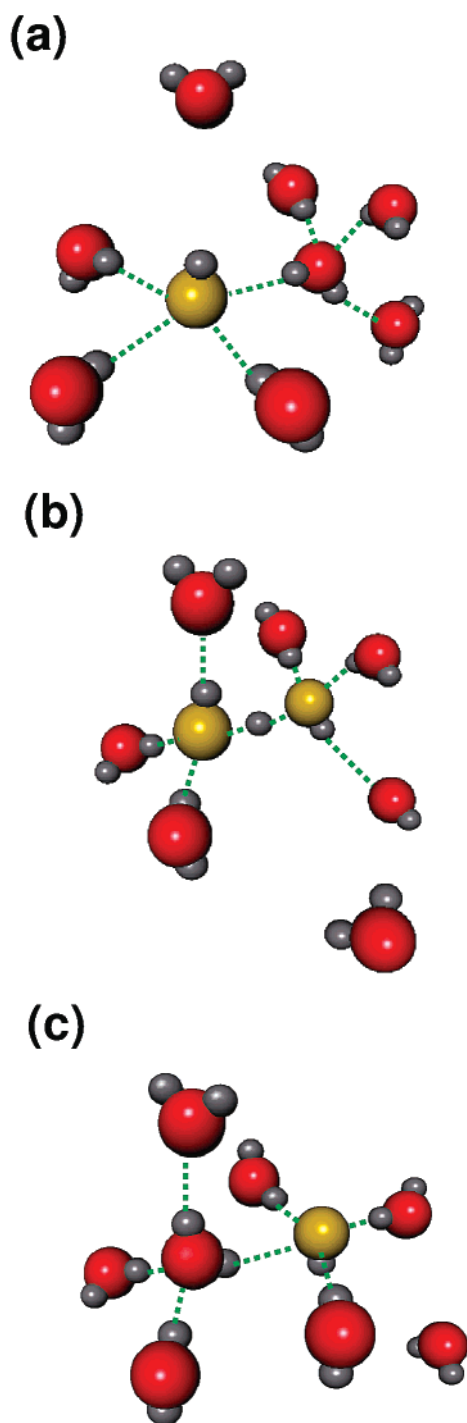


**Figure 2.** Illustration of the structural diffusion mechanism of  $\text{OH}^-$  in water<sup>31</sup> (see Figure 1 for color coding). In panel (a), the anion begins in a coordination pattern in which the  $\text{OH}^-$  oxygen accepts four hydrogen bonds in its first solvation shell in a planar arrangement forming the  $\text{H}_5\text{O}_4^+$  structure. The panel also shows the full 4-fold coordination pattern of one of the first solvation shell waters as well as a nearby solvent water. In panel (b), a first solvation shell hydrogen bond breaking even leaves the  $\text{OH}^-$  oxygen 3-fold coordinated, forming the  $\text{H}_3\text{O}_4^+$  structure. This causes a shrinking of the three hydrogen bonds in the first solvation shell. In this state, the  $\text{OH}^-$  hydrogen can form a weak hydrogen bond with a neighboring solvent molecule. If this occurs, the  $\text{OH}^-$  is coordinated like a water molecule, and a proton transfer event from one of the waters coordinating the  $\text{OH}^-$  oxygen can occur. In panel (c), the “gate closes” if, after the proton transfer, the newly formed  $\text{OH}^-$  captures a hydrogen bond to complete the  $\text{H}_5\text{O}_5^+$  structure. Although this process is shown using the water released from the second solvation shell in panel (b), it could be any nearby solvent water.

interpretation of the spectra is possible. Indeed, comparison to experimental spectroscopic data is a more sensitive test of the present *ab initio* approach. Moreover, it is also important to ask whether the transport mechanism and measured spectra are sensitive to concentration and, if so, whether different interpretations of experimental data in terms of high and low concentration transport mechanisms are needed. Indeed, the fact that the molar conductivity of an electrolyte solution decreases as concentration increases<sup>52,53</sup> suggests such a possibility, or, at least, some modification of the low concentration transport mechanism in the high concentration limit.

To investigate these issues and provide a more consistent interpretation of the existing experimental data in terms of a transport mechanism, we have undertaken an *ab initio* molecular dynamics (MD) study of concentration effects in an aqueous KOH solution. In an *ab initio* MD simulation, internuclear forces are computed “on the fly” from electronic structure calculations as the simulation proceeds.<sup>54</sup> The goal of this study is to investigate the effect of concentration on a directly measurable quantity, namely, the IR spectrum, as well as on the proton transport mechanism. In particular, it will be shown (i) that the computed IR spectrum is sensitive to concentration effects, (ii) that the average coordination of  $\text{OH}^-$  is only slightly lower at high concentration than at low concentration and the same solvation complexes exist at both concentrations, (iii) that the coordination of ordinary water molecules is approximately 3 compared to the bulk value of 4, (iv) that although the IR spectra are different at different concentrations, the structural diffusion mechanism is found to be the same at high and low concentration but that the structural diffusion process is considerably slower at high concentration, and (v) that the reduced water coordination is largely responsible for the slowing of the proton transport process. Points (iv) and (v) are consistent with the lower observed molar conductivity of electrolyte solutions at high concentration.<sup>52,53</sup>

This paper is organized as follows. In section 2, we describe the basic computational methodology and details of the present simulations. In section 3, we review the procedure for obtaining the IR spectra and present our computed spectra at both high and low concentrations. In section 4, we present an analysis and interpretation of the computed spectra. In section 5, we perform the analysis which demonstrates that the mechanism of structural diffusion is the same and compare the time scales for the process at the two concentrations. Further discussion and conclusions are presented in section 6.

## 2. Methodology

All simulations were performed using aqueous KOD solutions rather than KOH in order to reduce the importance of quantum effects arising from a classical treatment of the nuclei. Despite this, our nomenclature shall be to use “D” when describing spectroscopic features but “H” rather than “D” in describing structural properties as well as specific species and complexes. *Ab initio* MD simulations of an aqueous KOD solution at 13 and 1.5 M concentration were carried out at 300 K using the Car–Parrinello algorithm.<sup>54</sup> The high concentration system consisted of 27 water molecules and 8 dissociated KODs in a 10.15 Å periodic box, while the low concentration consisted of 32 waters and 1 dissociated KOD in a 10.25 Å periodic box. The electronic structure was represented using the Kohn–Sham (KS) formulation of the density functional theory (DFT) within the generalized gradient approximation (GGA) based on the B–LYP<sup>55,56</sup> exchange and correlation functional. The KS orbitals were expanded in a plane wave basis up to a cutoff of 70 Ry.



Core electrons were replaced by the norm-conserving pseudo-potentials of Troullier and Martins.<sup>57</sup> For potassium, a semi-core pseudopotential was employed. The high concentration system was equilibrated for 2.3 ps using the Nosé–Hoover chain approach<sup>58</sup> followed by 7.5 ps of data collection at constant energy. The low concentration system was similarly equilibrated for 2 ps followed by 10 ps of data collection. In both systems, a fictitious electron mass parameter (which has units of energy  $\times$  time<sup>2</sup>) of 600 au was employed. All simulations were performed using the CPMD code<sup>59</sup> on 12–16 processors of an IBM SP2.

### 3. IR Spectra

The procedure for calculating the IR spectrum in an ab initio MD simulation is described in detail elsewhere.<sup>60–62</sup> Here, we briefly review the technique. The IR absorption coefficient,  $\alpha(\omega)$ , at frequency  $\omega$  can be computed using linear response theory from the autocorrelation function of the total electric dipole moment,  $\mathbf{M}(t)$ , via<sup>63</sup>

$$\alpha(\omega)n(\omega) = \frac{4\pi\omega \tanh(\beta\hbar\omega/2)}{3\hbar c V} \int_{-\infty}^{\infty} dt e^{-i\omega t} \langle \mathbf{M}(t) \cdot \mathbf{M}(0) \rangle \quad (1)$$

where  $n(\omega)$  is the refractive index,  $c$  is the speed of light in vacuum,  $V$  is the system volume, and  $\beta = 1/k_B T$ . The total dipole moment consists of both ionic and electronic contributions. While the former can be computed straightforwardly, the latter cannot because the quantum mechanical position operator is not well defined for an infinite periodic system.<sup>61</sup> This difficulty has been solved using the so-called Berry phase approach<sup>60,61</sup> according to which the electronic contribution to the dipole moment for a cubic supercell at the  $\Gamma$ -point is given by

$$\mathbf{M}_{\text{elec}}^{(\gamma)} = -\frac{eL}{\pi} \text{Im} \ln \det(R^{(\gamma)}) \quad (2)$$

where  $e$  is the charge on the electron and  $\gamma$  indexes the three spatial components and the matrix  $R^{(\gamma)}$  is given by

$$R_{ij}^{(\gamma)} = \langle \psi_i | e^{-2\pi i r_\gamma / L} | \psi_j \rangle \quad (3)$$

Here,  $r_\gamma = x, y, z$  for  $\gamma = 1, 2, 3$ , respectively, and  $|\psi_i\rangle$  is the  $i$ th Kohn–Sham orbital.

In general, run lengths are too short to compute the IR spectrum by direct Fourier transformation of the autocorrelation function. In this case, maximum entropy methods can be very useful as a means of extracting the spectrum. In the present case, a maximum entropy method based on the 260-point Levinson algorithm<sup>64</sup> was employed. It should be noted that the computed spectra were not found to be sensitive to the order of the maximum-entropy algorithm; essentially the same result was obtained with 220, 240, 260, and 280 points. The calculated IR spectra for the high and low concentrations are presented in Figure 3. For the high concentration, the calculated spectrum agrees well with the measured spectrum of a 13.4 m solution reported in ref 42 and shown in inset (b) of Figure 3. The shift of the peaks in the computed spectrum to lower frequencies relative to those of the measured spectrum is due to the use of KOD rather than KOH in the simulations. This fact also leads to sharper peaks in the computed spectrum than in the measured KOH spectrum because of the lack of quantum broadening of the peaks. However, it is clear that all of the features of the measured spectrum are obtained in the computed spectrum. To our knowledge, no measurement of the low concentration

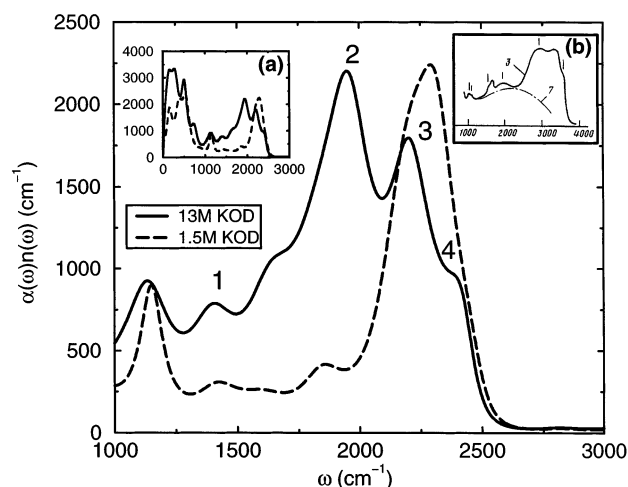


**Figure 3.** Computed infrared absorption spectrum in aqueous KOD solution at concentrations of 13 M (solid line) and 1.5 M (dashed line) (cf. eq 1) for the frequency range 1000  $\text{cm}^{-1}$  to 3000  $\text{cm}^{-1}$ . Inset (a) shows the spectrum over the full frequency range. Inset (b) shows the experimental spectrum for 14 M KOH solution from ref 42. The peak labels on the 13 M spectrum are referred to in the text.

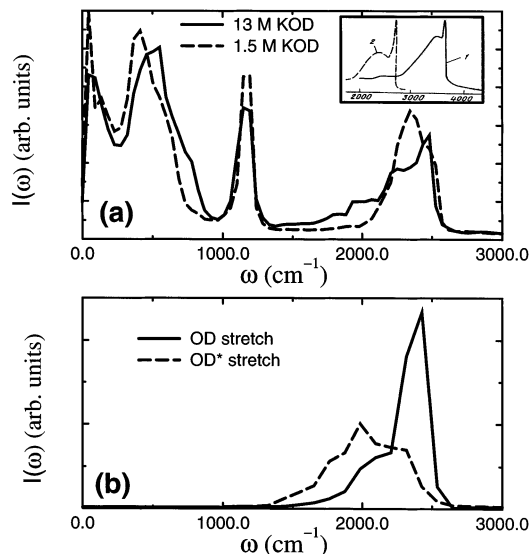


**Figure 4.** (a) Power spectra of the total velocity autocorrelation functions of aqueous KOD solutions at 13 M (solid line) and 1.5 M (dashed line) concentration. The inset shows the experimental Raman spectrum of 14 M NaOD (dashed line) and 14 M KOH (solid line) solution.<sup>42</sup> (b) Power spectra of the OD stretch velocity autocorrelation functions in 13 M KOD solution for water molecules in the first shell donating hydrogen bonds to the OD<sup>−</sup> oxygen. The dashed line shows the power spectrum for the OD bonds directly hydrogen-bonded to the OD<sup>−</sup> oxygen (OD\*) and the solid line shows the other OD bond spectrum (OD).

spectrum has yet been reported; however, the computed spectrum is only slightly different from the IR spectrum of pure water measured in ref 42 and computed in ref 62, as would be expected for a relatively low concentration solution. Here, the spectra are presented only for the frequency range 1000–3000  $\text{cm}^{-1}$  since it is this part that is most important for understanding solvation structures and the transport mechanism. Inset (b) in Figure 3 shows the spectra obtained over the full frequency range. Most importantly, there is a substantial difference between the high concentration and low concentration spectra. In particular, the high concentration spectrum shows more structure in the frequency range of interest. The frequencies at the peaks 1, 2, and 4 indicated in Figure 3 are 1410, 1950, and 2400  $\text{cm}^{-1}$ ,

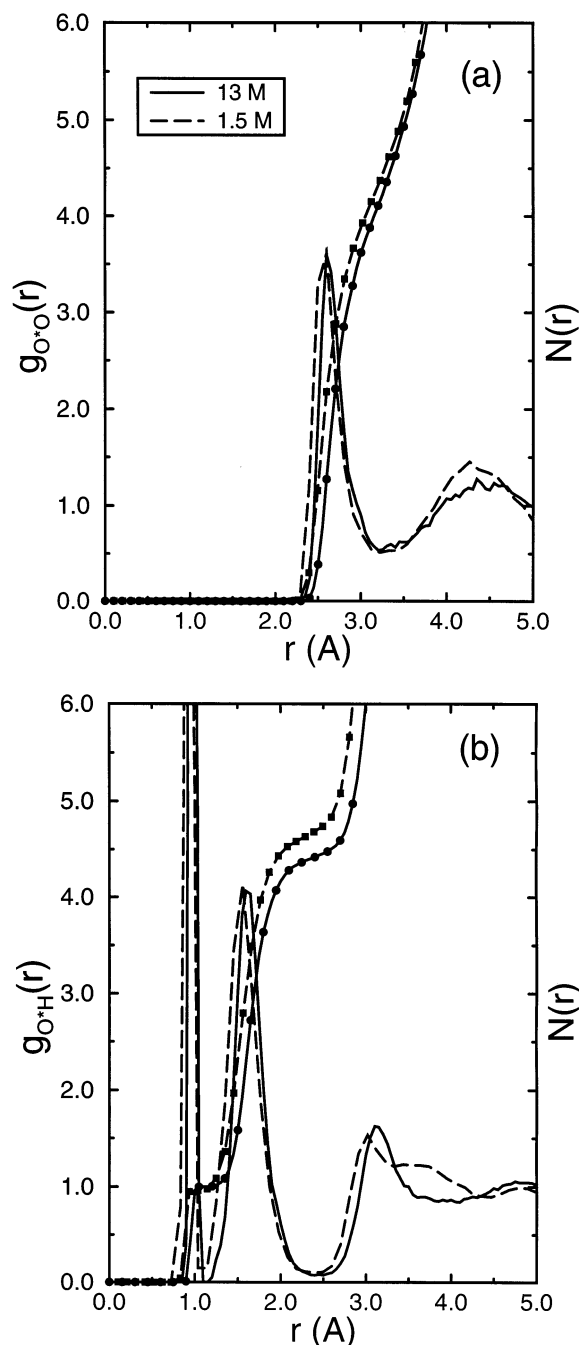


**Figure 5.** Total O\*O (a) and O\*H (b) radial distribution functions (RDF) (see text for definition of O\*) and, on the same scale, integrated coordination numbers. The solid lines and solid lines with filled circles show RDFs and coordination numbers at 13 M concentration, respectively, and the dashed lines and dashed lines with filled squares show the same at 1.5 M concentration.

respectively. The corresponding reported IR values in ref 42 are 1440, 2140, and 2650  $\text{cm}^{-1}$ , respectively. It can be seen that the two sets of values are in reasonable agreement. In ref 42, a particular interpretation of these peaks is presented. There, it is proposed that the peak at 1440  $\text{cm}^{-1}$  (computed: 1410  $\text{cm}^{-1}$ ) is due to the stretch of the OD bond donated to the hydroxide oxygen by first solvation shell waters. The peak at 2140  $\text{cm}^{-1}$  (computed: 1950  $\text{cm}^{-1}$ ) is assigned to the stretching of the other OD bond of these first solvation shell molecules. Finally, the shoulder at 2650  $\text{cm}^{-1}$  (computed: 2400  $\text{cm}^{-1}$ ) is associated with a free OD stretch in hydroxide moieties. Not unexpectedly, these features are largely suppressed in the low concentration spectrum. However, they are apparent as a slight

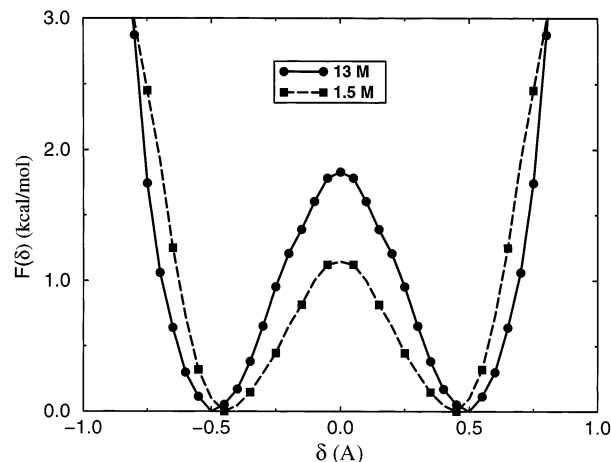


**Figure 6.** Free energy profiles of the proton transfer reaction coordinate (cf eq 5 and text following). The solid line with filled circles is the free energy profile for the 13 M solution and the dashed line with filled squares is the profile for the 1.5 M solution.

shoulder on the low-frequency side of the stretch band and a small peak at 1950  $\text{cm}^{-1}$ . To check these assignments, we present the power spectra of the total velocity autocorrelation function

$$I(\omega) = \int_{-\infty}^{\infty} dt e^{i\omega t} \frac{1}{N} \sum_{i=1}^N \langle \mathbf{v}_i(0) \cdot \mathbf{v}_i(t) \rangle \quad (4)$$

where  $N$  is the total number of atoms in the system, in Figure 4a. We also show the power spectra corresponding to the two OD stretches of the first solvation shell waters described above in Figure 4b. These power spectra show clearly that the stretch frequencies of the OD bonds pointing toward the hydroxide oxygen from the coordinating waters are red shifted compared to the other OD stretches of these coordinating waters (these are denoted OD\* in Figure 4). However, the peak of the OD\* power spectrum corresponds to the 1950  $\text{cm}^{-1}$  peak in the IR spectrum, whereas the OD power spectrum partially overlaps with the peak 3 of the IR spectrum, suggesting a different assignment of the peaks than that reported in ref 42. Finally, the full power spectrum shows that the stretch band is broad at both concentrations and that, at high concentration, there is a relatively prominent signal due to the hydroxide OD stretch, which appears only as a shoulder in the low concentration spectrum. Remarkably, this high concentration feature is similar to the prominent Raman peak<sup>42</sup> shown in the inset of Figure 4 (clearly, however, the power spectrum peak heights cannot be directly correlated with Raman intensities). As noted above, the computed high concentration spectrum agrees well with the measured spectrum.<sup>42</sup> However, as we shall see in the next section, the microscopic picture that emerges from the simulation of the proton transport mechanism is very different from that of the proton hole mechanism.

#### 4. Analysis and Interpretation of the Spectra

To determine what the IR spectra in the previous section indicate about the solvation structures and their role in the OH<sup>-</sup> transport process, we begin by looking at the radial distribution functions with respect to the hydroxide oxygens. Denoting the latter as O\*, the O\*O and O\*H radial distribution functions at both concentrations are presented in Figure 5. Also shown in the figure are the integrated coordination numbers. It should be noted that the identities of the O\* oxygens change constantly due to the transport process. The figure shows that the

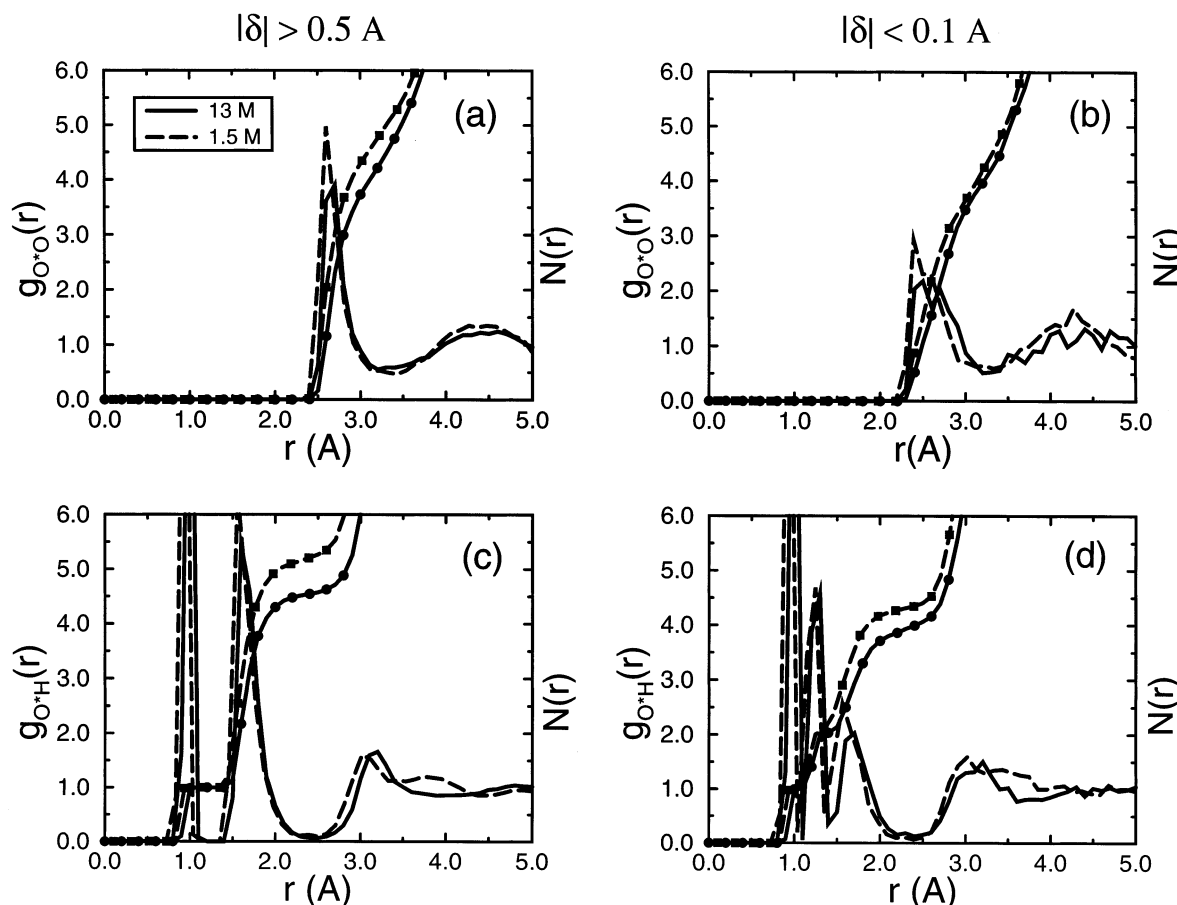


**Figure 7.** O\*O and O\*H radial distribution functions (RDFs) and, on the same scale, integrated coordination numbers for configurations with  $|\delta| > 0.5$  Å (a and c) and  $|\delta| < 0.1$  Å (b and d). The solid lines and solid lines with filled circles show RDFs and coordination numbers at 13 M concentration, respectively, and the dashed lines and dashed lines with filled squares show the same at 1.5 M concentration.

coordination of O\* at high concentration is only slightly smaller than in the low concentration case (4.3 vs 4.5). To examine the solvation structures that give rise to these coordination numbers and identify their role in the proton transport process at each concentration, we first define a proton transfer reaction coordinate as follows: Each OH<sup>-</sup> defect (denoted O\*H', where H' is the covalently bonded hydrogen to O\*) is located and the waters in the first solvation shell identified. For each hydrogen bond, an asymmetric stretch coordinate

$$\tilde{\delta} = d_{\text{O}^*\text{H}} - d_{\text{OH}} \quad (5)$$

is computed. From among these, we identify the hydrogen bond with the smallest  $\tilde{\delta}$  as the “most active” hydrogen bond or the hydrogen bond that is most likely to experience a proton transfer event.<sup>25</sup> The associated asymmetric stretch, denoted simply  $\delta$ , is then chosen as a proton transfer reaction coordinate. In the high concentration case, there will be such a coordinate for each OH<sup>-</sup> in the system. Thus, by examining the O\*O and O\*H radial distribution functions for small and large values of  $\delta$ , it is possible to identify the solvation structures that emerge when a proton is transferred from a first solvation shell water to the hydroxide and when the proton is well localized on first solvation shell water. To identify these regimes, we first examine the free energy profile of  $\delta$  computed from

$$F(\delta) = -k_{\text{B}}T \ln P(\delta) \quad (6)$$

where  $P(\delta)$  is the probability distribution function of  $\delta$ . The free energy profiles are shown in Figure 6. These profiles show

that there is a small free energy barrier to proton transfer in both cases (1.3 kcal/mol at 1.5 M concentration and 1.8 kcal/mol at 13 M concentration), a point to which we shall return shortly. Thus, while the average concentration of H<sub>3</sub>O<sub>2</sub><sup>-</sup> complexes is higher in the 13 M solution, the free energy profiles suggest that the average lifetime of any given H<sub>3</sub>O<sub>2</sub><sup>-</sup> complex is shorter at high concentration than at low concentration. The figure also shows that a value of  $|\delta| < 0.1$  Å is within the barrier region of the profile, while  $|\delta| > 0.5$  Å is near or beyond the location of the minima.

Therefore, using these two  $|\delta|$  regimes, we show, in Figure 7, the O\*O and O\*H radial distribution functions and integrated coordination numbers for  $|\delta| < 0.1$  Å and  $|\delta| > 0.5$  Å. The figure, together with visual inspection of the trajectories, reveals that, at both concentrations, when  $|\delta| > 0.5$  Å, the relevant solvation structure is the 4-fold coordinated state H<sub>9</sub>O<sub>5</sub><sup>-</sup>, in which O\* accepts four hydrogen bonds in a planar arrangement. In particular, the O\*H coordination numbers show a clear plateau at  $N_{\text{O}^*\text{H}} = 5$  for  $|\delta| > 0.5$  Å in the low concentration case. This number comprises the covalently bonded hydrogen, H', and the hydrogens donated by waters in the first solvation shell of O\*. The O\*H coordination number in the high concentration case for  $|\delta| > 0.5$  Å is about 4.6, which arises from a mixture of H<sub>9</sub>O<sub>5</sub><sup>-</sup> and distorted H<sub>7</sub>O<sub>4</sub><sup>-</sup> (planar rather than tetrahedral) complexes. Such high coordination states have also been observed for amide ions in liquid ammonia,<sup>51</sup> and an explanation of this phenomenon has been offered previously<sup>51</sup> based on examination of electron localization functions.<sup>65</sup> When  $|\delta| < 0.1$  Å, the O\*H coordination is found to decrease at both

concentrations to approximately 3, suggesting that, during proton transfer, the tetrahedral tricoordinate  $\text{H}_7\text{O}_4^-$  structure is dominant. Note, however, that the  $\text{O}^*\text{O}$  coordination number at  $|\delta| < 0.1 \text{ \AA}$  is still approximately 4, indicating that, in addition to the three waters donating hydrogen bonds to  $\text{O}^*$ , a fourth solvation shell member is present. Comparing Figure 7a and b, it is clear that this fourth member does not donate a hydrogen bond to  $\text{O}^*$ .

Interestingly, the measured Raman spectrum of a 13.4 m NaOD solution shows a sharp peak at  $2660 \text{ cm}^{-1}$ , while measured IR spectra show only a weak shoulder at  $2650 \text{ cm}^{-1}$  (corresponding to the shoulder near  $2500 \text{ cm}^{-1}$  in Figure 3). As noted earlier, previous interpretations of this difference<sup>39</sup> are that the  $\text{H}_3\text{O}_2^-$  complex is actually highly stable in aqueous basic solutions and that the hydrogens of the two OH moieties in the complex do not donate hydrogen bonds to water molecules. This is thought to explain the sharp peak in the Raman spectrum that occurs at the free OH stretch frequency, and the symmetry of this complex is thought to explain weakness of the IR signal due to the  $\text{O}^*\text{H}'$  stretch (the two OH moieties point in opposite directions and, therefore, the change in their dipole moments tend to cancel each other). The free energy profiles in Figure 6 show, however, that the symmetric  $\text{H}_3\text{O}_2^-$  complex is actually a transient complex that is necessarily visited when the proton is transferred. We have recently shown that when actual hydrogen is used and quantum effects are included, the 1.3 kcal/mol barrier observed in the low concentration case is reduced to approximately 0.34 kcal/mol, suggesting that the  $\text{H}_3\text{O}_2^-$  complex is still a transient complex. Moreover, we have also recently shown that, at low concentration, the hydroxide ion can donate a hydrogen bond to a neighboring water, and that this hydrogen bond plays an important role in the proton transfer process,<sup>31</sup> as noted in section 1. To demonstrate that this is also the case at high concentration, we plot, in Figure 8, the  $\text{H}'\text{O}$  radial distribution function in the two  $|\delta|$  regions described above at both concentrations. The most important feature of this plot is a peak near  $r = 2 \text{ \AA}$ , which is prominent at both concentrations for  $|\delta| < 0.1 \text{ \AA}$  and is considerably less prominent for  $|\delta| > 0.5 \text{ \AA}$ . This peak corresponds to a weak hydrogen bond between the hydroxide hydrogen,  $\text{H}'$ , and a neighboring water molecule. This  $\text{H}'\text{O}$  hydrogen bond, together with the reduction in coordination of  $\text{O}^*$  from 4 to 3 by first solvation shell hydrogen bond breaking, leaves the hydroxide moiety with a coordination pattern that closely resembles that of an ordinary water molecule. In this state,  $\text{O}^*$  can easily accept a proton from a coordinating water molecule, since, after proton transfer, the newly formed water molecule is in a proper, 4-fold tetrahedral coordination state.

Given that the  $\text{H}_3\text{O}_2^-$  complex is a transient species at both concentrations, that the hydroxide hydrogen can form weak hydrogen bonds, and that the computed high concentration IR spectrum agrees well with experiment, it is clear that another interpretation of the weakness of the hydroxide stretch signal near  $2500 \text{ cm}^{-1}$  in the IR spectrum is needed. First, we note that the sharp signal in the Raman spectrum at  $2660 \text{ cm}^{-1}$ ,<sup>42</sup> which occurs just to the right of the peak of the water stretching band, is a result of the relatively high polarizability of the hydroxide anion. Moreover, the change in the polarizability upon excitation would necessarily be entirely along the  $\text{O}^*\text{H}'$  bond axis. By contrast, the dipole moment of  $\text{OH}^-$  in the gas phase is approximately 0.9 D compared to 1.8 D for  $\text{H}_2\text{O}$  in the gas phase. Since the average dipole moment of water in the liquid is  $\mu \sim 3.0 \text{ D}$ ,<sup>66</sup> it is reasonable to expect that the dipole moment of  $\text{OH}^-$  in a 13 M KOH solution would be considerably less

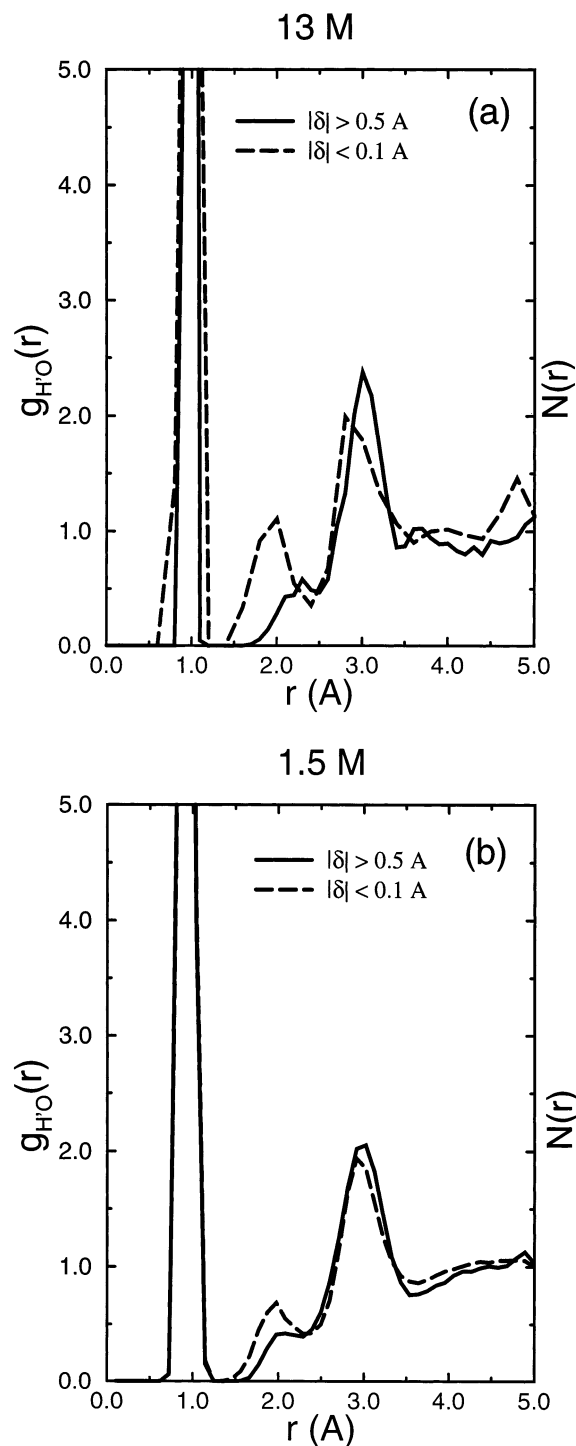


**Figure 8.**  $\text{H}'\text{O}$  radial distribution functions (where  $\text{H}'$  is the hydroxide hydrogen) for  $|\delta| > 0.5 \text{ \AA}$  (solid lines) and  $|\delta| < 0.1 \text{ \AA}$  (dashed lines) at (a) 13 M concentration and (b) 1.5 M concentration.

than that of water and, therefore, would be less likely to produce a strong infrared signal compared to its coordinating waters. Moreover, it is reasonable to expect that the change in the dipole moment for  $\text{OH}^-$  would be largely swamped by the coordinating waters because of the high coordination of  $\text{OH}^-$ . However, it is important to point out that the hydroxide stretch signal is, nevertheless, more prominent in the high concentration IR spectrum than it is in the low concentration spectrum. These simple observations provide an explanation of the difference between the Raman and IR spectra that is consistent with the observed proton transport mechanism in the simulations.



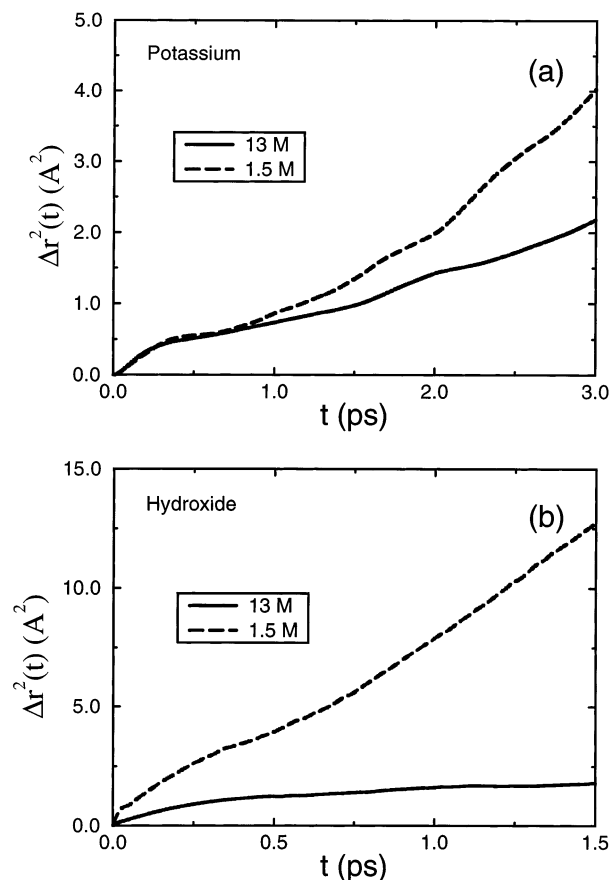


**Figure 9.** Mean square displacements for potassium ions (a) and  $\text{OH}^-$  ions (b) in 13 M KOD solution (solid lines) and 1.5 M KOD solution (dashed lines).

### 5. Comparison of Proton Transport Time Scales

It is well known that the molar conductivity of an electrolyte solution decreases with increasing concentration<sup>52,53</sup> (the decrease at high concentration tends to be a weaker function of concentration than it is at very low concentration where Debye–Hückel theory is valid<sup>52,53</sup>). Given this, we would expect that the mobilities of both the  $\text{K}^+$  and  $\text{OH}^-$  should be noticeably lower at the high concentration than at low concentration. To demonstrate that this is indeed the case, we plot the mean square displacement of both  $\text{K}^+$  and  $\text{OH}^-$  in Figure 9. Note that the mean square displacement of  $\text{OH}^-$  also accounts for the fact that the identity of  $\text{O}^*$  constantly changes. The figure clearly shows that the rate of diffusion of both ions is considerably faster at low concentration than at high concentration.

The reduced mobility of  $\text{K}^+$  at high concentration can be understood largely on hydrodynamic grounds. Indeed, the KO radial distribution functions and integrated coordination numbers shown in Figure 10a demonstrate that, at low concentration, the  $\text{K}^+$  ion is in a proper 6-fold coordination state but that at high concentration, the radial distribution function does not exhibit a well-defined minimum after the first peak, indicating a less structured solvation shell and a higher effective coordination number and, thus, suggesting a greater hydrodynamic drag force. Moreover, the  $\text{KO}^*$  radial distribution function at high concentration (Figure 10b), also shown in the figure, indicates that there is more structure between the ionic species.

The reduced mobility of  $\text{OH}^-$  is somewhat more difficult to rationalize given that it possesses a fast structural diffusion mechanism. From a microscopic viewpoint, there must be something slowing down the Grotthuss process at high con-

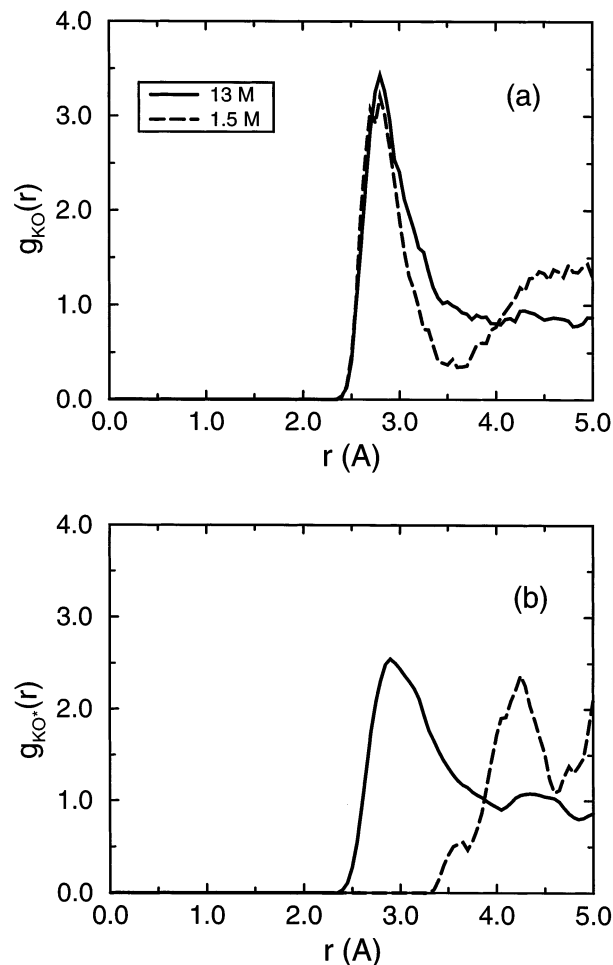


**Figure 10.** (a) KO radial distribution functions at 13 M concentration (solid line) and at 1.5 M concentration (dashed line). (b)  $\text{KO}^*$  radial distribution functions at 13 M concentration (solid line) and at 1.5 M concentration (dashed line).

centration. To investigate what this additional influence might be, consider the OO and OH radial distribution functions and integrated coordination numbers of the water molecule in the first solvation shell of  $\text{OH}^-$  that transfers its proton to  $\text{O}^*$ . We examine these distribution functions in the small  $|\delta|$  regime ( $|\delta| < 0.1$   $\text{\AA}$ ) in Figure 11. For comparison, we also show the  $\text{O}^*\text{O}$  and  $\text{O}^*\text{H}$  radial distribution functions in the same  $|\delta|$  regime in the figure. The figure shows that at small  $|\delta|$ , when the proton is located midway between the two oxygens, the environment around each OH moiety is nearly identical. In particular, the coordination of each moiety is 4, i.e., the correct water coordination number.

Consider, next, the OO and OH radial distribution functions and integrated coordination numbers of all bulk water molecules at each concentration. These are shown in Figure 12. The figure shows that, in the high concentration solution, the structure of water is significantly perturbed. In particular, the first OO peak is shifted to the left and secondary peaks are largely washed out. Second, both plots show that the coordination number is reduced from 4 (the correct bulk value) at low concentration to 3 at high concentration. Thus, on average, bulk water is undercoordinated at high concentration, most likely due to the high coordination numbers of both potassium and hydroxide ions in the system. Figure 12 suggests that, at low concentration, water molecules in the first solvation shell of  $\text{O}^*$  are generally in the correct solvation state to give up one of their protons and form the symmetric environment suggested by Figure 11.



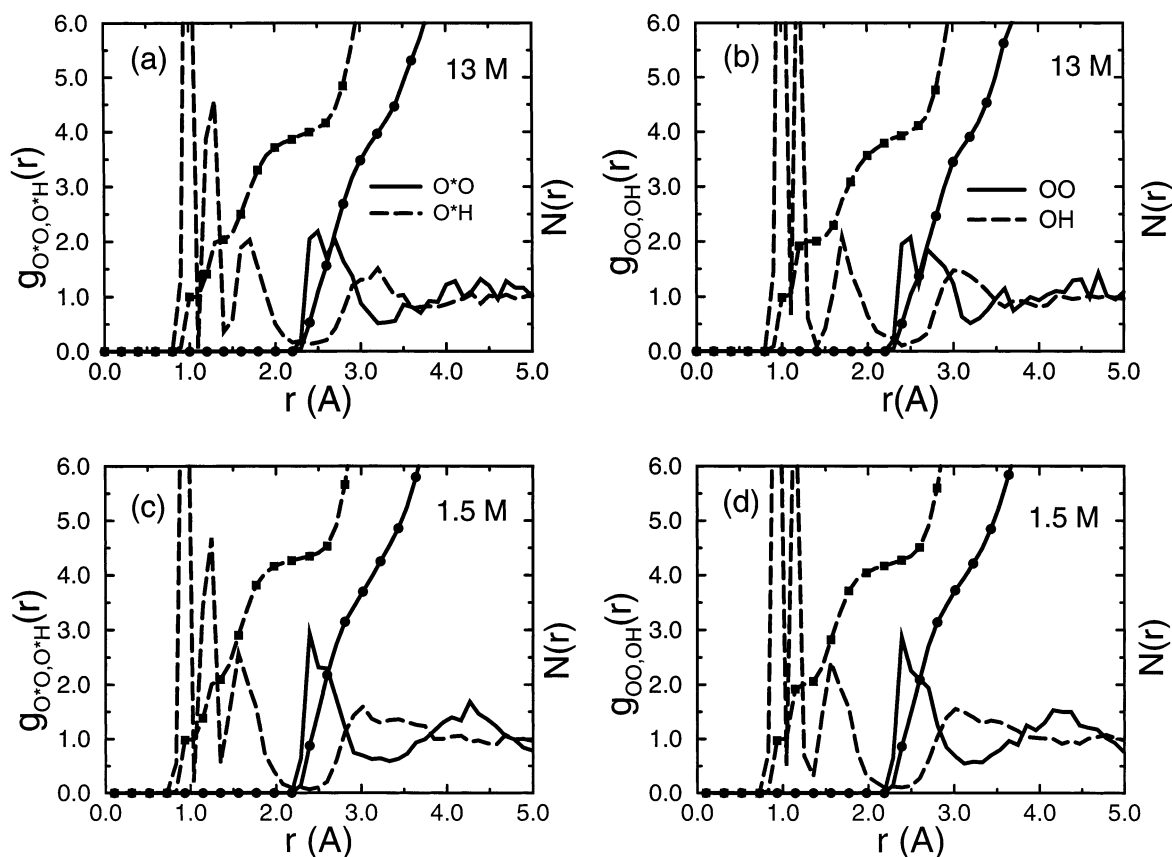


**Figure 11.** O\*O and O\*H radial distribution functions (RDFs) and, on the same scale, integrated coordination numbers for  $|\delta| < 0.1 \text{ \AA}$  at (a) 13 M concentration and (c) 1.5 M concentration. The solid lines and solid lines with filled circles show RDFs and coordination numbers at 13 M concentration, respectively, and the dashed lines and dashed lines with filled squares show the same at 1.5 M concentration. Panels (c) and (d) show the same RDFs and integrated coordination numbers in 13 and 1.5 M solutions for the first solvation shell water molecule that transfers its proton to the hydroxide oxygen, O\*O.

By contrast, at high concentration, the average coordination of bulk water molecules is approximately 3. This means that an additional step in the proton transport mechanism is required, namely, as Figures 2 and 12 suggest, the transferring water molecule must first acquire an additional hydrogen bond in order to complete its solvation shell before it can give up one of its protons to O\*. This additional step is likely strongly rate limiting as a consequence of the general lack of “free” water in the system to form the required hydrogen bond. Thus, while the microscopic transport mechanism is the same at both concentrations, an additional step required at high concentration is likely a significant factor in the slowing down of the process and, therefore, provides a plausible explanation of the observed reduction in molar conductivity at high concentration.

## Conclusions

The proton transport mechanism in dilute and concentrated KOH solutions has been investigated using *ab initio* molecular dynamics. Through these calculations, the IR spectra have been obtained and found to agree well with measured spectra in the high concentration case. However, the microscopic picture of charged defect transport that has emerged from the simulations at both high and low concentration is very different from the previously assumed “proton hole” mechanism.<sup>39</sup> This finding indicates that previous interpretations of the spectral data are likely not correct. It has been shown that the microscopic transport mechanism, illustrated in Figure 2, is valid at both high and low concentrations. Thus, while it had been previously assumed that the features of the IR spectrum, particularly in comparison with the measured Raman spectrum, indicated a stable

H<sub>3</sub>O<sup>2-</sup> solvation structure, the picture that emerges from the present simulations shows that this is not the case and, therefore, that a different interpretation of the spectrum is needed.

A new interpretation consistent with the structural diffusion mechanism is that the change in the dipole moment of OH<sup>-</sup> in solution is largely washed out due to its high coordination number. This high coordination does not affect the Raman spectrum as strongly because of the relatively high polarizability of OH<sup>-</sup> and the fact that the change in the polarizability is entirely along the OH<sup>-</sup> bond axis.

It has also been demonstrated that the mobility of both K<sup>+</sup> and OH<sup>-</sup> ions is greatly reduced at high concentration, a fact that is consistent with the observed reduction in molar conductivity of electrolyte solutions with increasing concentration. Finally, it has been shown that the microscopic origin of the reduced mobility of OH<sup>-</sup> is the reduced coordination of water in the system. The fact that water molecules are, on the average, undercoordinated gives rise to an additional step in the Grotthuss transport process, namely, the completion of the solvation shell by acquisition of one additional hydrogen bond by the water that transfers one of its protons to the hydroxide ion. This additional step is strongly rate limiting because of the lack of “free” water available at high concentration for effecting this solvation shell completion step.

We feel that our study emphasizes the difficulties associated with attempting to intuit microscopic mechanisms purely on the basis of an interpretation of a limited set of experimental data without any access to the microscopic dynamics of the system. It also underscores the fact that H<sub>3</sub>O<sup>+</sup> and OH<sup>-</sup> are chemically different so that it is not possible to deduce the transport

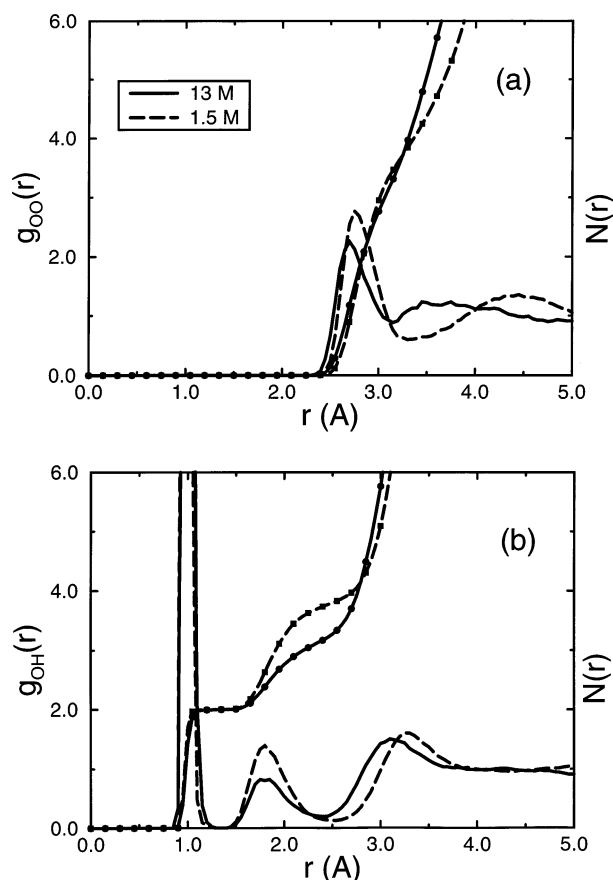


**Figure 12.** OO and OH radial distribution functions (RDFs) and, on the same scale, integrated coordination numbers for bulk water at 13 M concentration and 1.5 M concentration. Panel (a) shows the OO RDFs and integrated coordination numbers, and panel (b) shows the OH RDFs and integrated coordination numbers. The solid lines and solid lines with filled circles show RDFs and coordination numbers at 13 M concentration, respectively, and the dashed lines and dashed lines with filled squares show the same for the 1.5 M concentration.

mechanism of the latter from that of the former via a proton hole notion. We hope that our study highlights the rich variety of behavior associated with microscopic origins of concentration dependence of conductivity in both acidic and basic solutions and will prompt further investigation into these important phenomena. In particular, the present findings suggest that high concentration solutions could be used to validate the proposed  $\text{OH}^-$  transport mechanism<sup>31</sup> experimentally.

**Acknowledgment.** The authors acknowledge Peter Minary and Hans Schelvis for many useful discussions. This work was supported by NSF CHE-9875824, NSF EIA-0081307, NSF CHE-0121375 and the Research Corporation RI0218. All of the simulations were performed using supercomputing resources made available under NRAC allocation MCA00N011S.

## References and Notes

- (1) Nagle, J. F.; Scott, H. L. *Biochim. Biophys. Acta* **1978**, *513*, 236.
- (2) Nichols, J. W.; Deamer, D. W. *Proc. Natl. Acad. Sci. U.S.A.* **1980**, *77*, 2038.
- (3) Paula, S.; Volkov, A. G.; Hoek, A. N. V.; Haines, T. H.; Deamer, D. W. *Biophys. J.* **1996**, *70*, 339.
- (4) Haines, T. H. *Prog. Lipid Res.* **2001**, *40*, 299.
- (5) Zahn, D.; Brickmann, J. *Phys. Chem. Chem. Phys.* **2001**, *3*, 848.
- (6) In *1st European PEFC Forum*, 2–6 July, Lucerne, Switzerland; European Fuel Cell Forum: Oberrohrdorf, Switzerland, 2001.
- (7) In *Proceedings of the International Conference 'The Fuel Cell Home'*, 2–6 July, Lucerne, Switzerland; Nurdin, M. Ed.; European Fuel Cell Forum: Lucerne, Switzerland, 2001.
- (8) Meiboom, S. *J. Chem. Phys.* **1961**, *34*, 375.
- (9) Hyman, H. H.; Quarterman, L. A.; Kilpatrick, M.; Katz, J. J. *J. Phys. Chem.* **1961**, *65*, 123.
- (10) Eigen, M. *Angew. Chem., Intl. Ed.* **1964**, *3*, 1.
- (11) Gillespie, R. J.; Moss, K. C. *J. Chem. Soc. A* **1961**, *38*, 1170.
- (12) Montrose, C. J.; Bucaro, J. A.; Marshall-Coakley, J.; Litovitz, T. A. *J. Chem. Phys.* **1974**, *60*, 5025.
- (13) Zundel, G. In *The Hydrogen Bond, Recent Developments in Theory and Experiments*; Schuster, P., Zundel, G., Sandorfy, C., Eds.; North-Holland: Amsterdam, 1976; pp 687–766.
- (14) Bonnet, B.; Mascherpa, G. *Inorg. Chem.* **1980**, *19*, 785.
- (15) Halle, B.; Karlstroem, G. *J. Chem. Soc., Faraday Trans. 2* **1983**, *79*, 1047.
- (16) Tuckerman, M. E.; Laasonen, K.; Sprik, M.; Parrinello, M. *J. Phys. Chem.* **1995**, *99*, 5749.
- (17) Tuckerman, M. E.; Laasonen, K.; Sprik, M.; Parrinello, M. *J. Chem. Phys.* **1995**, *103*, 150.
- (18) Agmon, N. *Chem. Phys. Lett.* **1995**, *244*, 456.
- (19) Lobaugh, J.; Voth, G. A. *J. Chem. Phys.* **1996**, *104*, 2056.
- (20) Vuilleumier, R.; Borgis, D. *J. Mol. Struct.* **1997**, *437*, 555.
- (21) Agmon, N. *J. Mol. Liq.* **1997**, *73*, 513.
- (22) Vuilleumier, R.; Borgis, D. *J. Phys. Chem. B* **1998**, *102*, 4261.
- (23) Sagnella, D.; Tuckerman, M. E. *J. Chem. Phys.* **1998**, *108*, 2073.
- (24) Trout, B. L.; Parrinello, M. *Chem. Phys. Lett.* **1998**, *288*, 343.
- (25) Marx, D.; Tuckerman, M. E.; Hutter, J.; Parrinello, M. *Nature* **1999**, *367*, 601.
- (26) Vuilleumier, F.; Borgis, D. *J. Chem. Phys.* **1999**, *111*, 4251.
- (27) Schmitt, U. W.; Voth, G. A. *J. Chem. Phys.* **1999**, *111*, 9361.
- (28) Agmon, N. *Isr. J. Chem.* **1999**, *39*, 493.
- (29) Marx, D.; Tuckerman, M. E.; Parrinello, M. *J. Phys.: Condens. Matter* **2000**, *12*, A153.
- (30) Geissler, P. L.; Dellago, C.; Chandler, D.; Hutter, J.; Parrinello, M. *Science* **2001**, *291*, 2121.
- (31) Tuckerman, M. E.; Marx, D.; Parrinello, M. *Nature* **2002**, *417*, 925.
- (32) de Grotthuss, C. J. T. *Ann. Chim.* **1806**, *LVIII*, 54.
- (33) Jones, M. *Organic Chemistry*, 2nd ed.; W. W. Norton and Company: New York, 1997.
- (34) Khalifah, R. G. *Proc. Natl. Acad. Sci. U.S.A.* **1973**, *70*, 1986.
- (35) Woolley, P. *Nature (London)* **1975**, *258*, 677.
- (36) Yand, X.; Castleman, A. W., Jr. *J. Am. Chem. Soc.* **1991**, *113*, 6766.
- (37) Danneel, H. Z. *Elektrochem.* **1905**, *16*, 249.
- (38) Hueckel, E. Z. *Elektrochem.* **1928**, *34*, 546.
- (39) Agmon, N. *Chem. Phys. Lett.* **2000**, *319*, 247.
- (40) Busing, W. R.; Hornig, D. F. *J. Chem. Phys.* **1961**, *65*, 284.
- (41) Zatespina, P. N. *J. Struct. Chem.* **1971**, *12*, 894.
- (42) Librovich, N. B.; Maiorov, V. D. *Russ. J. Phys. Chem.* **1982**, *56*, 380.
- (43) Chaudhuri, C.; Wang, Y. S.; Jiang, J. C.; Lee, Y. T.; Chang, H. C.; Heidner-Schatteburg, G. *Mol. Phys.* **2001**, *1161*, 213.
- (44) Buchner, R.; Hefter, G.; May, P. M.; Sipos, P. *J. Phys. Chem. B* **1999**, *103*, 11186.
- (45) Novoa, J. J.; Mota, F.; del Valle, C. P.; Planas, M. *J. Phys. Chem. A* **1997**, *101*, 7842.
- (46) Marx, D.; Parrinello, M. *Z. Phys. B* **1994**, *95*, 143.
- (47) Tuckerman, M.; Marx, D.; Klein, M.; Parrinello, M. *J. Chem. Phys.* **1996**, *104*, 5579.
- (48) Loewenstein, A.; Szoek, A. *J. Am. Chem. Soc.* **1962**, *84*, 1151.
- (49) Luz, Z.; Meiboom, S. *J. Am. Chem. Soc.* **1964**, *86*, 4768.
- (50) Morrone, J. A.; Tuckerman, M. E. *J. Chem. Phys.* in press.
- (51) Liu, Y.; Tuckerman, M. E. *J. Phys. Chem. B* **2001**, *105*, 6598.
- (52) Bagotsky, V. S. *Fundamentals of Electrochemistry*; Plenum Press: New York, 1993.
- (53) Koryta, J.; Dvorak, J.; Kavan, L. *Principles of Electrochemistry*; John Wiley & Sons: Chichester, 1993.
- (54) Car, R.; Parrinello, M. *Phys. Rev. Lett.* **1985**, *55*, 2471.
- (55) Becke, A. D. *Phys. Rev. A* **1988**, *38*, 3098.
- (56) Lee, C.; Yang, W.; Parr, R. C. *Phys. Rev. B* **1988**, *37*, 785.
- (57) Troullier, N.; Martins, J. L. *Phys. Rev. B* **1991**, *43*, 1993.
- (58) Martyna, G.; Tuckerman, M.; Klein, M. *J. Chem. Phys.* **1992**, *97*, 2635.
- (59) Hutter, J.; Ballone, P.; Bernasconi, M.; Focher, P.; Foiss, E.; Goedecker, S.; Marx, D.; Parrinello, M.; Tuckerman, M. E. CPMD Version 3.0h, Max-Planck Institut für Festkörperforschung und IBM Zurich Research Laboratory, 1995–1996.
- (60) King-Smith, R. D.; Vanderbilt, D. *Phys. Rev. B* **1993**, *47*, 1651.
- (61) Resta, R. *Rev. Mod. Phys.* **1994**, *66*, 899.
- (62) Silvestrelli, P. L.; Bernasconi, M.; Parrinello, M. *Chem. Phys. Lett.* **1997**, *277*, 478.
- (63) Guillot, B. *J. Chem. Phys.* **1991**, *95*, 1543.
- (64) Nailong, W. *The Maximum Entropy Method*; Springer: Berlin, 1997.
- (65) Becke, A. D.; Edgecombe, K. E. *J. Chem. Phys.* **1990**, *92*, 5397.
- (66) Silvestrelli, P. L.; Parrinello, M. *Phys. Rev. Lett.* **1999**, *82*, 3308.